Gadalla, Mahmoud; Kannan, Jeevananthan; Tekgul, Bulut; Karimkashi, Shervin; Kaario, Ossi; Vuorinen, Ville

Large-eddy simulation of tri-fuel combustion

Published in:
International Journal of Hydrogen Energy

DOI:
10.1016/j.ijhydene.2021.03.238

Published: 15/06/2021

Document Version
Publisher's PDF, also known as Version of record

Available online at www.sciencedirect.com

ScienceDirect

journal homepage: www.elsevier.com/locate/he

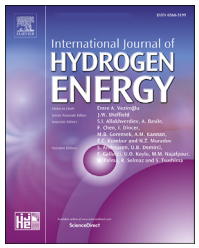

Large-eddy simulation of tri-fuel combustion: Diesel spray assisted ignition of methanol-hydrogen blends

Mahmoud Gadalla[*], *Jeevananthan Kannan*, *Bulut Tekgül*, *Shervin Karimkashi*, *Ossi Kaario*, *Ville Vuorinen*

Department of Mechanical Engineering, Aalto University School of Engineering, Otakaari 4, 02150, Espoo, Finland

HIGHLIGHTS

- Tri-fuel (TF) ignition system comprising diesel, methanol, and hydrogen is studied.
- Dual-fuel diesel/methanol system poses narrow temperature window for smooth ignition.
- Adding hydrogen to the premixed charge advances IDT and avoids ambient autoignition.
- TF ignition modes are characterized with relevance to heat release rates.

ARTICLE INFO

Article history:
Received 27 October 2020
Received in revised form
28 March 2021
Accepted 29 March 2021
Available online 24 May 2021

Keywords:
Large-eddy simulation
Spray
Ignition
Diesel
Methanol
Hydrogen

ABSTRACT

Development of marine engines could largely benefit from the broader usage of methanol and hydrogen which are both potential energy carriers. Here, numerical results are presented on tri-fuel (TF) ignition using large-eddy simulation (LES) and finite-rate chemistry. Zero-dimensional (0D) and three-dimensional (3D) simulations for *n*-dodecane spray ignition of methanol/hydrogen blends are performed. 0D results reveal the beneficial role of hydrogen addition in facilitating methanol ignition. Based on LES, the following findings are reported: 1) Hydrogen promotes TF ignition, significantly for molar blending ratios $\beta_X = [H_2]/([H_2]+[CH_3OH]) \geq 0.8$. 2) For $\beta_X = 0$, unfavorable heat generation in ambient methanol is noted. We provide evidence that excessive hydrogen enrichment ($\beta_X \geq 0.94$) potentially avoids this behavior, consistent with 0D results. 3) Ignition delay time is advanced by 23–26% with shorter spray vapor penetrations (10–15%) through hydrogen mass blending ratios 0.25/0.5/1.0. 4) Last, adding hydrogen increases shares of lower and higher temperature chemistry modes to total heat release.

* *Corresponding author.*
E-mail address: mahmoud.gadalla@aalto.fi (M. Gadalla).

https://doi.org/10.1016/j.ijhydene.2021.03.238

Introduction

Using long-chain hydrocarbons in power generation has raised environmental concerns during the past few decades. These concerns are mainly due to the global (e.g. carbon dioxide, CO_2), and local (e.g. NOx and particulate matter) emissions of these fuels. More recently, novel mitigation strategies toward carbon-neutral energy [1] have been taken in different pathways, including decarbonization techniques [2] and chemical recycling of CO_2 [3]. In internal combustion engines (ICE), emerging in-cylinder combustion technologies have been introduced to cope with stringent emission regulations [4]. Moreover, the utilization of low carbon or carbon-neutral fuels and in particular renewable fuels have been extensively discussed as an effective measure to reduce engine emissions. The need for higher engine efficiency has placed compression ignition (CI) engines in the forefront of combustion research over spark ignition (SI).

Amongst modern combustion technologies that have been introduced in CI ICE context is the dual-fuel (DF) [5,6] concept. With relevance to the present study, in DF setup a lean mixture of low reactivity fuel (LRF) premixed with air, possibly combined with exhaust gas recirculation (EGR), is introduced to the cylinder through the intake manifold delivering the primary energy to the system. The lean condition of the premixed charge allows to achieve low temperature combustion while minimizing NOx and soot emissions [4]. The premixed charge is then ignited by a pilot high-reactivity fuel (HRF) which is directly injected into the engine cylinder at the end of compression stroke. With DF technology, renewable LRFs or their blends can be used in CI ICEs to enhance combustion performance while achieving low emissions.

In typical spray-assisted DF ignition systems, three consecutive stages are realized, particularly (i) liquid evaporation and turbulent mixing, (ii) low-temperature chemistry (LTC), and (iii) high-temperature chemistry (HTC), as detailed in Fig. 1. The near-nozzle region is characterized by a cool droplet-laden two-phase flow with large momentum and shear stresses, hence a strong turbulent mixing with hot ambient and subsequently liquid evaporation. Sufficiently downstream of the nozzle, a liquid phase terminates and vaporized HRF reacts with oxidizer while forming a volumetric LTC zone. The onset of LTC activation is referred to as the first-stage ignition (τ_1) and it is marked by the formation of alkylperoxy radicals, i.e. $C_{12}H_{25}O_2$ (RO_2), which denote early *n*-dodecane decomposition. Further downstream of the LTC region, a transition towards HTC is realized through successive production and consumption of intermediate species until the occurrence of high temperature pockets (i.e. ignition kernels) within the spray periphery. The onset of HTC is denoted as the second-stage ignition (τ_2) and the transition duration between τ_1 and τ_2 represents the chemical induction time.

Methanol (CH_3OH) and hydrogen (H_2) are among the most interesting LRFs with potential to be considered as emerging energy carriers in marine engines [8–11]. Several studies considered methanol in DF systems ignited by pilot diesel. For instance, experimental investigations of port-injected methanol concentration or diesel injection timing variation on various combustion metrics including ignition delay time (IDT) [12,13], combustion duration [13], combustion modes [14], and emission characteristics [15] at different loads have been conducted. Moreover, effects of combustion stability and cyclic variations by altering various parameters at different engine loads were investigated in Refs. [16,17]. On the numerical side, Li et al. [18] studied effects of diesel start of injection (SOI), methanol fraction, and initial in-cylinder temperature and concluded that methanol addition has outstanding advantages towards emission reduction and fuel economy. On a general note, by considering experimental and numerical literature, methanol has been considered as a potential candidate to reduce emissions while prolonging IDT.

Alternatively, hydrogen has been employed with diesel in the DF context. Experimental investigations on the effects of various parameters including engine load [19], EGR [20–22], intake air boost [22], hydrogen flow rate [23], and injection strategy [21,24] on combustion and emission characteristics

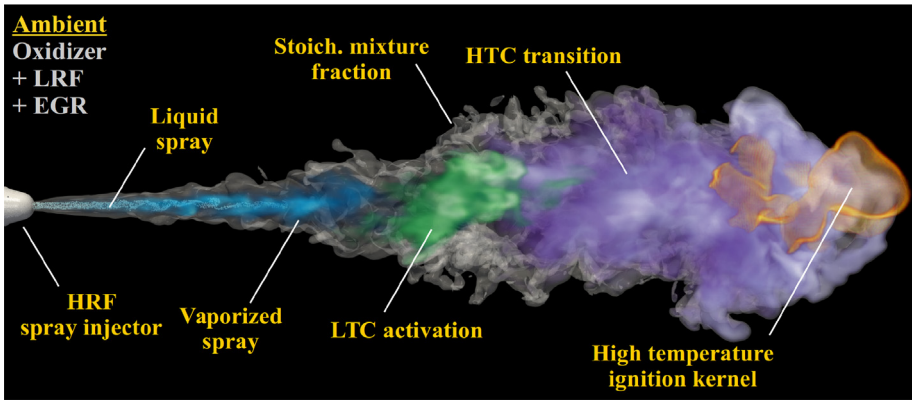

Fig. 1 – Volume rendering of typical stages in a spray-assisted dual-fuel ignition process, based on similar setup in Ref. [7] while replacing methane with methanol as LRF. Liquid (cyan) and vaporized (blue) sprays denote LPT droplets and gaseous phases, respectively. RO_2 (green) and OH (orange) radicals mark LTC activation and ignition kernels, respectively, while HTC transition (purple) is defined by H_2O_2 consumption rates. (For interpretation of the references to color in this figure legend, the reader is referred to the Web version of this article.)

were reported for various hydrogen shares. Numerically, the two successive works by Hosseini and Ahmadi [25,26] along with the work by Jabbr and Koylu [27] discussed the effects of hydrogen enrichment to the premixed charge. They noted that under optimal conditions, adding hydrogen reduces soot and greenhouse gas emissions while prolonging ignition delay, consistent with the discussions by Yuan et al. [28]. Moreover, the experimental works in Refs. [23,29] show that hydrogen addition prolongs ignition delay, whereas Lata et al. [30] studied ignition characteristics, concluding that IDT may be highly dependent on the thermophysical conditions of the charge. Further studies concerning the injection parameters sensitivity and variations of engine specifications are found in Refs. [31,32].

Despite their growing economy, utilization of pure methanol or hydrogen as LRF in DF CI engines has its own challenges compared with methane/diesel DF engines which provide robust combustion [6,33–36]. Perhaps the most important barriers to overcome are related to operating range limitations for methanol [8,14,37,38] and safety concerns for hydrogen [39]. According to the authors' early findings (see Section Background), methanol poses a narrow operating window for ambient temperature (T_{amb}) leading to smooth ignition. In specific, at high temperatures (T_{amb} = 1000 K) it may lead to a premixed ambient autoignition and subsequently, possible knock. Also, at low ambient temperatures (T_{amb} = 900 K) long ignition delays start to be problematic. According to Karimkashi et al. [40], blending hydrogen with methanol in the premixed charge can advance autoignition at 900 K. Such an approach was introduced as the tri-fuel (TF) concept. Although several TF studies have been conducted for various fuel blends, for instance Refs. [41,42] as well as in our recent study [43], a TF system comprising methanol/hydrogen/diesel has not yet been tested except for the mentioned analysis [40] which was restricted to zero-dimensional (0D) models.

It would be highly advantageous to broaden the operational window of methanol in order to avoid the premixed ambient autoignition [38]. The present study aims at providing, for the first time, detailed insights on the ignition characteristics associated with hydrogen-enriched mixture involving methanol, air and EGR while ignited by a pilot diesel spray. The overall objective is to explore the TF concept using three-dimensional (3D) large-eddy simulations (LES) together with Lagrangian particle tracking (LPT) and finite-rate chemistry. The particular objectives are stated as follows:

1. Use 0D modeling to explore the parameter space in terms of T_{amb}, ambient equivalence ratio (ϕ_{amb}), and the hydrogen-to-methanol blending ratio (β) to broaden the previous picture concerning *n*-dodecane/CH_3OH DF operational window.
2. Use 3D modeling to carry out a systematic sweep in β space focusing on the challenging conditions in terms of the mixture's ignitability that was previously noted for *n*-dodecane/methanol DF system.
3. Analyze the 3D LES data in order to understand the impact of hydrogen on the ignition characteristics with respect to IDT, ambient reactivity, and ignition modes.

Methodology and numerical framework

The present study employs a numerical framework that has been thoroughly validated in our previous works under non-reacting [44,45] and reacting [6] for SF ECN Spray A conditions. Furthermore, the numerical framework has been extensively used in various dual-fuel [6,33,34,46] and recently tri-fuel [43] studies. Validation of the modeling assumptions has been performed against the available ECN experimental data such as liquid and vapor penetrations, ignition delay time, flame lift-off, and evolution of key species, whereas validation of the chemical mechanism for methanol and hydrogen oxidation is presented in Appendix A. Grid independence on IDT for one of the considered TF cases is demonstrated in Appendix B. For a dispersed droplet-laden two-phase flow, compressible LES is utilized for the gaseous phase while the atomized liquid spray is modeled using LPT parcels. Furthermore, a finite-rate chemistry approach is used to calculate the chemical kinetics, with reaction source terms being introduced to the Eulerian governing equations. A brief description of the various modeling choices is presented in the subsections, while extensive modeling details are provided in Ref. [47].

Governing equations and turbulence modeling

The gaseous phase is described by the compressible Navier-Stokes equations. The corresponding Favre-filtered LES formulations for the conservation of mass, momentum, species, and enthalpy are all presented as:

$$\frac{\partial \overline{\rho}}{\partial t} + \nabla\cdot(\overline{\rho}\,\widetilde{\boldsymbol{u}}) = \overline{S}_{\rho}, \tag{1}$$

$$\frac{\partial \overline{\rho}\widetilde{\boldsymbol{u}}}{\partial t} + \nabla\cdot(\overline{\rho}\widetilde{\boldsymbol{u}}\otimes\widetilde{\boldsymbol{u}}) = \nabla\cdot\left(-\overline{p}I + \overline{\rho}\widetilde{\boldsymbol{u}}\otimes\widetilde{\boldsymbol{u}} - \overline{\rho}\widetilde{\boldsymbol{u}\otimes\boldsymbol{u}} + \overline{\boldsymbol{\tau}}\right) + \overline{S}_{\boldsymbol{u}}, \tag{2}$$

$$\frac{\partial(\overline{\rho}\widetilde{Y}_k)}{\partial t} + \nabla\cdot(\overline{\rho}\widetilde{\boldsymbol{u}}\widetilde{Y}_k) = \nabla\cdot\left(\overline{\rho}\widetilde{D}\nabla\widetilde{Y}_k + \overline{\rho}\widetilde{\boldsymbol{u}}\widetilde{Y}_k - \overline{\rho}\widetilde{\boldsymbol{u}Y}_k\right) + \overline{S}_{Y_k} + \overline{\dot{\omega}_k}, \tag{3}$$

$$\frac{\partial(\overline{\rho}\widetilde{h}_t)}{\partial t} + \nabla\cdot(\overline{\rho}\widetilde{\boldsymbol{u}}\widetilde{h}_t) = \frac{\partial \overline{p}}{\partial t} + \nabla\cdot\left(\overline{\rho}\widetilde{D}\nabla\widetilde{h}_s + \overline{\rho}\widetilde{\boldsymbol{u}}\widetilde{h}_s - \overline{\rho}\widetilde{\boldsymbol{u}h}_s\right) + \overline{S}_h + \overline{\dot{\omega}_h}, \tag{4}$$

where $\overline{\rho}$, $\widetilde{\boldsymbol{u}}$, $\overline{p}$, $\overline{\boldsymbol{\tau}}$, $\widetilde{Y}_k$, $\widetilde{D}$, $\widetilde{h}_s$, $\widetilde{h}_t$ denote the filtered density, velocity, pressure, viscous stress tensor, *k*th species mass fraction, mass diffusivity, sensible and total enthalpy, respectively. The overbar denotes an unfiltered ensemble average whereas the tilde operator denotes a density-weighted ensemble average, and the ($\otimes$) symbol refers to the outer product. The filtered source terms $\overline{S}_{\rho}$, $\overline{S}_{\boldsymbol{u}}$, $\overline{S}_{Y_k}$, $\overline{S}_h$ are introduced to couple liquid and gaseous phases with respect to mass, momentum, species, and energy, respectively. The chemical source terms $\overline{\dot{\omega}_k}$ and $\overline{\dot{\omega}_h}$ denote the respective species net production/consumption rate and heat release rate (HRR), and their implementation is discussed in Section Spray and combustion modeling.

Equations (1)–(4) are closed by thermodynamic and caloric state equations for ideal gas, and the resulting set of equations is numerically discretized using the finite volume method

(FVM) within OpenFOAM-6 framework [48]. The reacting PISO algorithm [49] is utilized for pressure-momentum coupling, whereas LES subgrid scale (SGS) terms, i.e. $(\widetilde{\bar{\rho}\bar{u}\bar{\psi}} - \bar{\rho}\widetilde{\bar{u}}\widetilde{\bar{\psi}})$ for some field variable ψ, are modeled using the implicit LES (ILES). Consistent with our previous studies, in this modeling procedure, a locally dissipative non-linear flux-limiting scheme developed by Jasak et al. [50] is employed with a control parameter value of 0.3 for the convective terms. Such an ILES approach has been thoroughly validated and applied by our group in various applications including reacting sprays [6,33,34,43,46,51], heat transfer [52,53], and two-phase flows [54,55]. For temporal integration, an implicit three time-level scheme is used, whereas diffusion terms are discretized via a second-order central scheme.

Spray and combustion modeling

The short liquid core and rapid atomization process typically associated with diesel sprays under engine-relevant conditions suggest modeling the dispersed liquid phase in the Lagrangian framework, without resolving the near-nozzle region. The no-breakup model approach is employed herein which assumes that droplets have already undergone primary and secondary atomization, and they are introduced to the system with a constant droplet diameter corresponding to stable Weber number ($We < 12$). Moreover, a cylindrical injection model is used which extends the standard OpenFOAM disc injection model into 3D by introducing droplets at random positions inside a cylindrical volume. Implementation procedures of the aforementioned models are discussed in Ref. [44]. Further aspects regarding mesh-parcel interaction [56], droplet dispersion [57] and droplet breakup [45] within OpenFOAM framework have been noted in the literature.

The chemical source term $\overline{\dot{\omega}_k}$, and subsequently $\overline{\dot{\omega}_h} = \Sigma_k \Delta h^0_{f,k} \overline{\dot{\omega}_k}$ with $\Delta h^0_{f,k}$ denoting kth species enthalpy of formation, are evaluated via direct integration of the finite-rate chemistry. An operator-splitting approach is used to separate the chemical and flow equations. Within a CFD timestep, the time change of thermo-chemical composition is evaluated by solving a separate system of stiff ordinary differential equations (ODE) using an extrapolation-based semi-implicit Euler algorithm. An analytic formulation of the ODE system Jacobian matrix is generated using the open-source library *pyJac* [58] and coupled with OpenFOAM for the ODE iterative solution procedure. Furthermore, a dynamic load balancing using Message Passing Interface (MPI) protocol is employed to enhance the computational performance by distributing the chemistry computational load equally amongst all available processors. Finally, a reference cell approach is used to compute chemical source terms within the spray periphery, while the chemistry of the ambient premixed charge is evaluated only for one computational cell and then mapped to others, hence a further increase in the dynamic load balancing performance.

Considering chemical reaction kinetics, the skeletal mechanism developed by Frassoldati et al. [59], called POLIMI-96 hereafter, involving 96 species and 993 reactions is utilized. With relevance to the ECN Spray A conditions, this mechanism was previously employed for LES analysis of DF ignition with methane [6] and it was experimentally validated against methanol [60] and hydrogen [40] oxidation, which is also herein performed in Appendix A. We also acknowledge the ignition delay time sensitivity towards a chemical mechanism choice, as further discussed in Appendix A.

The effect of turbulence-chemistry interactions (TCI) is considered via a first order closure hypothesis for reaction rates evaluation without SGS terms. The underlying argument is that induced turbulence and high shear stresses due to the continuous, high momentum spray injection lead to intense mixing with reduced chemical stratification levels. Therefore, a perfectly stirred reactor (PSR) approach within the relatively small computational cells is argued to be sufficient in predicting the ignition characteristics [33,34,61], which is further supported by a mesh sensitivity analysis in Appendix B. Several LES studies using such a simplified approach with finite-rate chemistry have shown promising results with agreement to experimental data [62–64]. Moreover, It has been previously demonstrated that a TCI model has less influence on ignition delay time compared to transient spray flame dynamics and stabilization effects [34,65]. The details of ignition front propagation under spray-assisted configurations are subjects of a follow-up study.

Homogeneous reactor modeling

For the 0D analysis conducted in the present study, the open source library Cantera [66] is used with a general schematic diagram outlined in Fig. 2a. Here, separate streams for cold HRF (*n*-dodecane, $T = 363$ K) and hot EGR and oxidizer including LRFs ($T_{amb} = 900$ K) are adiabatically mixed in a constant pressure (equivalent to $\rho = 22.8$ kg/m^3 for the mentioned T_{amb}) homogeneous reactor. The LRFs/oxidizer stream is kept at a lean condition whereas a premixing ratio between HRF and the oxidizer/LRF/EGR mixture is defined based on Bilger's definition [67] for mixture fraction (Z). In the presence of HRF, IDT of a DF or TF system is herein sampled at various Z values with relevance to the adiabatic mixing line concept [68] by progressively adding HRF to the mixture.

A blending ratio between the employed LRFs (CH_3OH and H_2) is defined by the parameter (β) as follows

$$\beta = \frac{[H_2]}{[CH_3OH] + [H_2]}, \tag{5}$$

which is based on either molar (β_X) or mass (β_Y) concentrations. It is worth noting that the light and diffusive H_2 molecules lead to a significant reduction in the mixture's mean molecular weight while increasing its volumetric average. This is demonstrated in Fig. 2b wherein, for instance, a hydrogen blending mass ratio of 20% is about 80% by volume. Additionally, from the ideal gas law, a mixture's pressure increases with β due to the reduced mean molecular weight with a fixed temperature and density. Such a pressure rise is roughly 17.2% from $\beta = 0$ to $\beta = 1$.

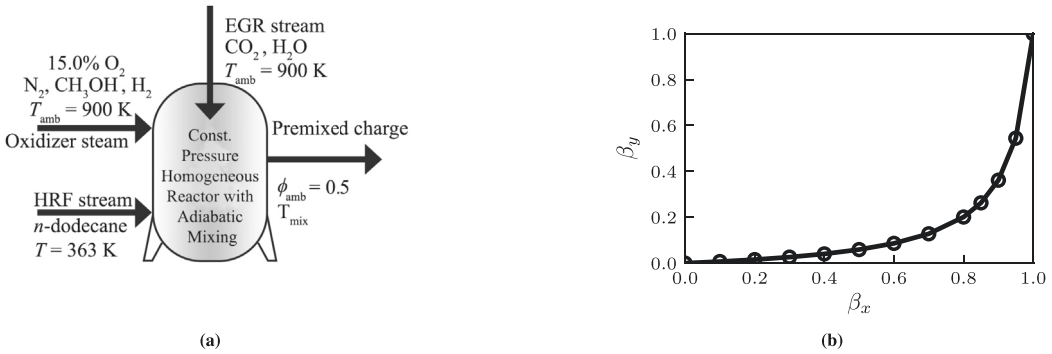

Fig. 2 – (a) Schematic of the homogeneous reactor setup utilized in the 0D analysis with $\rho = 22.8$ kg/m^3. (b) Blending ratio in molar (β_X) versus mass (β_Y) basis, which reflects the significantly large specific volume of H_2 compared with CH_3OH.

Table 1 – TF simulation test cases compared with DF and SF ECN Spray A.

	SF	DF	TF-80	TF-85	TF-90	TF-95	TF-100
T_{amb} [K]	900	900	900	900	900	900	900
T_{liq} [K]	363	363	363	363	363	363	363
ρ [Kg/m^3]	22.8	22.8	22.8	22.8	22.8	22.8	22.8
β_X	–	0.0	0.80	0.85	0.90	0.95	1.0
O_2 [%, mol]	15.0	15.0	15.0	15.0	15.0	15.0	15.0
N_2 [%, mol]	75.15	70.729	65.677	64.948	64.098	63.093	61.888
CO_2 [%, mol]	6.23	5.864	5.445	5.384	5.314	5.231	5.131
H_2O [%, mol]	3.62	3.407	3.164	3.129	3.088	3.039	2.981
CH_3OH [%, mol]	0.0	5.0	2.143	1.731	1.25	0.682	0.0
H_2 [%, mol]	0.0	0.0	8.571	9.808	11.25	12.955	15.0
ϕ_{amb}	0.0	0.5	0.5	0.5	0.5	0.5	0.5
$Z_{st.}$	0.0435	0.0229	0.0249	0.0252	0.0256	0.0261	0.0266

LES configuration and test cases

Five test cases are considered for LES analysis, in which a blend of hydrogen and methanol is varied between $\beta_X = 0.8$ and 1.0. This range is chosen because the effect of hydrogen for $\beta_X < 0.8$ was noted to be rather subtle. The LRFs are premixed with oxidizer and EGR to create a homogeneous lean charge ($\phi_{amb} = 0.5$) that is ignited by a pilot *n*-dodecane spray. The operating conditions for spray injection and ambient gas follow those for the ECN Spray A. A summary of the operating conditions and mixture composition for the considered TF test cases is presented in Table 1 in comparison to the SF and DF counterparts, while $Z_{st.}$ denotes stoichiometric mixture fraction. A justification for the selected TF cases is provided in Section Parametric analysis in homogeneous reactor models.

The computational domain volume is equivalent to Sandia combustion vessel [69] utilized for ECN diesel spray experiments. As depicted in Fig. 3, first, the domain is discretized into a background hexahedral mesh of cell size $\Delta = 1000$ μm (R1). Then, successive spatial refinement layers based on cell-splitting approach are applied to properly resolve the spray turbulence and the ignition event with a 125 μm resolution (R2), yielding approximately 11 million cells.

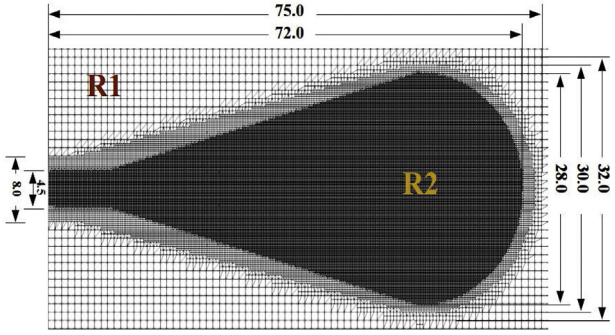

Fig. 3 – Grid discretization in the near-nozzle region for the studied LES (dimensions in mm). Spatial resolutions are indicated by R1 and R2 which correspond to cell sizes of 1000 and 125 μm respectively.

It is worth mentioning that the present mesh resolution, previously employed in Ref. [45], is selected to achieve an adequate balance between the resolved length scales for TCI and the computational burden due to relatively long IDTs associated with methanol utilization. As shown in Appendix B, a conducted mesh sensitivity analysis demonstrates that global ignition characteristics are fairly grid insensitive compared to 62.5 μm resolution, while the computational load

(in terms of CPU-hours) is reduced by a factor of approximately 20.

Furthermore, regarding grid requirements for the spray, we note a spatial separation between the liquid spray and the chemistry. This implies a termination of the liquid phase usually before the onset of chemical reactions. In fact, the modeling success of the present LES/LPT framework is verified by comparisons to ECN experimental data of liquid length and vapor penetration of the spray [44,45], which are prerequisites for successful ignition characteristics prediction.

Results and discussions

Background

The present study is motivated by the authors' early works on LES of *n*-dodecane/methanol DF configuration at different ambient temperatures. The injection and ambient conditions were similar to the ECN Spray A, whereas spray, chemistry, and turbulence submodels were all consistent with those presented in Section Methodology and numerical framework. Considering our results, a narrow window of proper T_{amb} leading to a smooth ignition is realized. As depicted in Fig. 4, this narrow window is bounded by different ignition behaviors represented in a i) premixed ambient autoignition at $T_{amb} = 1000$ K, and ii) considerably long ignition delay time (exceeding 3 ms) at $T_{amb} = 900$ K. Based on these results, a solution is required to extend the operating window for methanol utilization as an LRF in DF CI engines context.

Amongst possible options to control methanol ignitability would be varying ϕ_{amb} of the premixed ambient (methanol, oxidizer, and EGR) in the combustion vessel, or blending methanol with another LRF. Recently, Karimkashi et al. [40] reported that hydrogen enrichment to the premixed charge at $T_{amb} = 900$ K imposes promoting effects on ignition, hence a shorter IDT, which was explained by a reaction sensitivity analysis. In Section Parametric analysis in homogeneous reactor models, we investigate effects of various ambient conditions (T_{amb} and ϕ_{amb} of the premixed ambient as well as blending methanol with hydrogen) on IDT using 0D homogeneous reactor models. The overall aim is to 1) modify the premixed charge IDT such that it becomes substantially different than that for HRF to avoid premixed ambient autoignition, and 2) advance the IDT of *n*-dodecane/methanol/oxidizer/EGR mixture at $T_{amb} = 900$ K to enhance ignition robustness. Thereafter, in Section LES analysis of the selected conditions is provided.

Parametric analysis in homogeneous reactor models

Based on the configuration described in Section Homogeneous reactor modeling for a 0D homogeneous reactor model, in this section we perform parametric sweep investigations for SF, DF, and TF homogeneous mixtures as discussed in the following.

SF: HRF and LRFs ignition delay time comparison

As a first analysis, ignition delay times of HRF and LRFs considered in this study are demonstrated. Fig. 5 depicts IDTs using POLIMI-96 mechanism compared with other mechanisms developed by Petersen et al. [70] and Klippenstein et al. [71] under engine relevant conditions, while initial conditions are presented in Table 2. Ignition patterns of *n*-dodecane and methane present typical HRF and LRF behaviors, respectively, through the entire temperature interval. It is shown that CH_3OH demonstrates a higher reactivity with almost one order of magnitude smaller IDT compared with H_2. Accordingly, CH_3OH can be considered an HRF at higher temperature values, with comparable reactivities to *n*-dodecane, hence suggesting its possible utilization in CI engines as an HRF through high compression ratios [72].

DF: effects of ambient temperature and LRF

The following parametric investigation provides a temperature sweep in Z space such that a homogeneous mixture comprising LRF, oxidizer, and EGR is prepared with $T_{amb} = 900$, 950, or 1000 K, while a fixed $T = 363$ K is set for the HRF (*n*-dodecane) stream. In Fig. 6a wherein CH_3OH is the LRF, it is observed that increasing T_{amb} advances IDT for all Z values while the most reactive mixture fraction (Z_{MR}) gets richer. Moreover, there is a noted inflection in the IDT curve at leaner Z when $T_{amb} = 950$ or 1000 K. Such an inflection behavior is related to the comparable reactivities of CH_3OH and *n*-dodecane at higher T_{amb}, c.f. Fig. 5. At Z = 0, i.e. without HRF, the homogenous mixture has a temperature value of T_{amb} and it autoignites at relatively small time scales which is considered unfavorable. By successively adding cold HRF to the mixture, its temperature drops and thereby IDT is prolonged. After having sufficient HRF in the

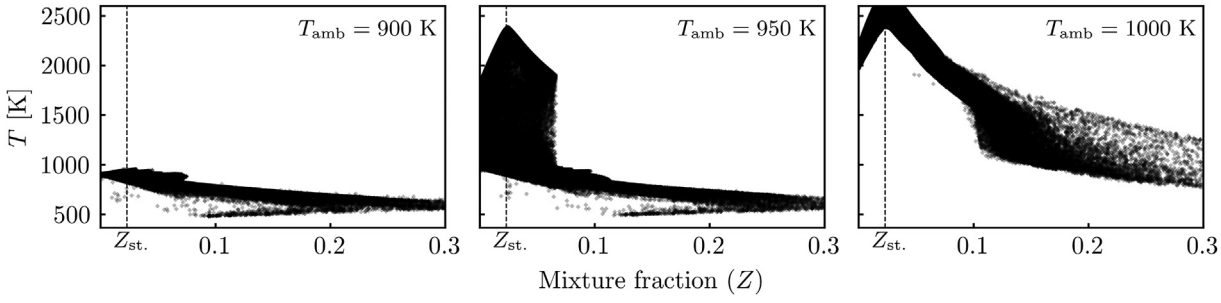

Fig. 4 – Scatter plots of temperature data points in Z space corresponding to 3D LES of *n*-dodecane/methanol DF at three ambient temperature levels. Plots indicate a narrow window for smooth ignition concentrated about $T_{amb} = 950$ K, while ambient (Z = 0) autoignition is observed at $T_{amb} = 1000$ K and no ignition is observed at $T_{amb} = 900$ K. Snapshots correspond to $1.2\tau_2$ except for $T_{amb} = 900$ K which is sampled after 3 ms.

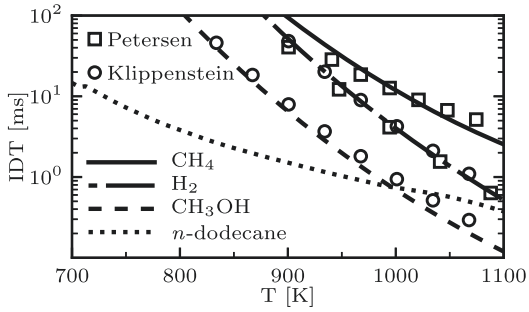

Fig. 5 – IDT of SF homogeneous mixture. Methanol has stronger reactivity than hydrogen. Although *n*-dodecane is a typical HRF, at higher temperatures methanol presents comparable reactivity.

Table 2 – Initial conditions of the SF premixed charge in homogeneous reactor model.

	SF-CH_3OH	SF-H_2
T [K]	varied	varied
ρ [Kg/m^3]	22.8	22.8
O_2 [%, mol]	15.0	15.0
N_2 [%, mol]	70.729	61.888
CO_2 [%, mol]	5.864	5.131
H_2O [%, mol]	3.407	2.981
CH_3OH [%, mol]	5.0	0.0
H_2 [%, mol]	0.0	15.0
ϕ_{amb}	0.5	0.5

mixture to compensate temperature drop effects, IDT is reduced again with Z and thereby resulting into an inflection behavior close to stoichiometry.

When H_2 is considered as the LRF in Fig. 6b instead of CH_3OH, shorter IDT values are achieved at the same temperature levels. Also, no inflections are observed and autoignition seems to be avoided even at higher temperatures for the presented temporal range. Moreover, compared with Fig. 6a, at $T_{amb} = 900$ K the relatively richer $Z_{st.}$ and leaner Z_{MR} result in a smaller range of intermediate mixture fractions, which is relevant to 3D most reactive zones, i.e. within Z_{MR} and $Z_{st.}$ as discussed in Ref. [6]. These intermediate mixture fractions are mostly ignitable within 3 ms, in contrast to the case with CH_3OH that yields quite long IDTs while approaching stoichiometry. Therefore, with relevance to Ref. [40], replacing methanol with hydrogen as a primary LRF ignited by diesel will advance IDT while preserving a wider T_{amb} window for smooth ignition.

Ignitability map comprising T_{amb}, ϕ_{amb} and β effects

The previous analysis indicated that a DF mixture with hydrogen results into shorter IDTs in Z space while avoiding LRF autoignition, compared with a DF mixture utilizing methanol at the same ambient conditions. Starting from the latter DF mixture, other possibilities to advance IDT could be the reduction of LRF mass fraction (i.e. smaller ϕ_{amb}) or through partially replacing CH_3OH with H_2 (i.e. TF mixture [40]). The respective IDT plots in Z space are not herein shown for brevity. Instead, we present a phase diagram, depicted in Fig. 7, which denotes IDT(Z_{MR}) while varying the conditions T_{amb}, ϕ_{amb} and the methanol/hydrogen blending ratio β. The overall aim behind this ignitability map is to i) present combined effects of the aforementioned parameters on the mixture's IDT, ii) identify the range of conditions leading to possible autoignition in the premixed ambient without HRF, and iii) highlight candidate conditions for the homogeneous mixture that achieves smooth ignition with advanced IDT to undergo further analyses in 3D LES.

Starting from the conditions $T_{amb} = 900$ K and $\phi_{amb} = 0.5$ for *n*-dodecane/methanol DF setup resulting in IDT(Z_{MR})- = 0.71 ms, three pathways could advance IDT as discussed earlier, i.e. towards higher T_{amb}, lower ϕ_{amb}, or larger β. The dark dashed isoline in the diagram marks IDT = 0.5 ms, whereas the hatched and filled regions depict possible ambient autoignition without HRF in less than 2 ms (yellow) or 3 ms (orange), respectively, with relevance to the inflection behavior previously noted in Fig. 6a.

Typically, in spray-assisted DF ignition the aim is to achieve a controlled and robust ignition timing which is closely correlated with the spray injection timing. Such an approach eliminates undesired phenomena such as chances of spray

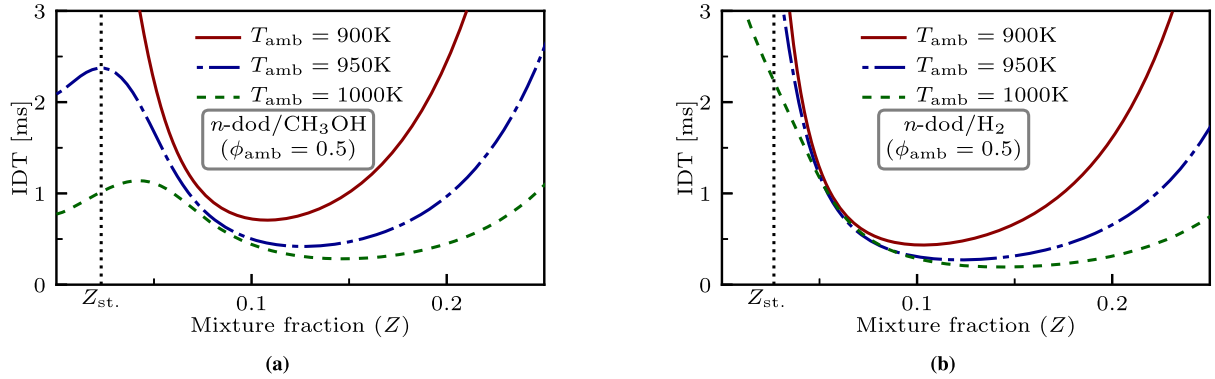

Fig. 6 – IDT of (a) *n*-dodecane/methanol, and (b) *n*-dodecane/hydrogen, DF homogeneous mixture in Z space at $\phi_{amb} = 0.5$ and varied T_{amb}. Replacing CH_3OH with H_2 as LRF advances IDT with a wider T_{amb} window for a smooth ignition. Ambient autoignition without HRF (Z = 0) for $\beta = 0$ is removed for $\beta = 1$ at higher temperatures.

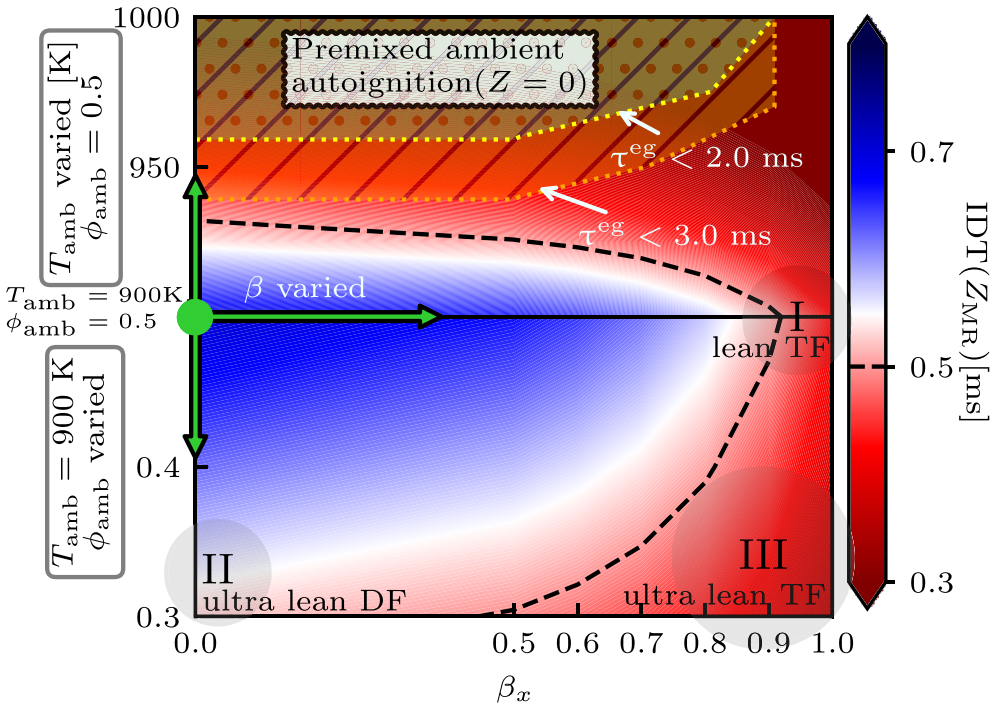

Fig. 7 – Ignitability map based on 0D homogeneous reactor simulations assuming the mixing line concept. The map denotes IDT(Z_{MR}) of the lean TF mixture (HRF, LRFs, oxidizer, and EGR) at various T_{amb}, ϕ_{amb}, and β conditions with fixed $\rho = 22.8$ kg/m^3. Hatched areas mark conditions resulting into premixed ambient autoignition without HRF. The diagram motivates the TF concept highlighting the benefit of H_2 as means to mitigate ambient autoignition while advancing IDT.

over-dilution, late combustion, or misfire. Moreover, Kahila et al. [6] reported that ignition delay time in 3D LES occurs almost 2–3 times later in time compared with 0D models. Therefore, those regions with longer IDTs than the IDT = 0.5 ms isoline could be considered unfavorable. In fact, we seek conditions for a homogeneous mixture such that, when employed for LES, it would i) be robustly ignited by the HRF spray and thereby avoiding possible spray over-dilution, and ii) provide a considerable time-scale separation of ignition delay times between LRFs blend and the HRF, hence mitigate the ambient autoignition.

After excluding unfavorable zones based on the phase diagram, three operating conditions indicated by zones I–III are considered. In particular, zone I depicts a lean ($\phi_{amb} = 0.5$) TF mixture ($\beta_X = 0.8$–1.0) whereas zones II and III note ultra lean ($\phi_{amb} \approx 0.3$) DF and TF mixtures, respectively. The benefit of blending H_2 with CH_3OH is two-fold: i) the lower reactivity of H_2 compared with CH_3OH promotes stabilization of the premixed ambient without HRF, c.f. Fig. 5, and ii) the *n*-dodecane reaction pathways were shown to impose promoting effects and higher OH consumption rates with hydrogen enrichment [40], hence, a shorter IDT is achieved. In the present study, zone I is chosen for 3D LES analysis, since the ultra lean nature of both zones II and III might lead to further complications considering ignition stability. In the following section, LES results of the chosen test cases are discussed, and the required H_2 quantity to promote IDT while mitigating the ambient reactivity is investigated. At this point, it is necessary to emphasize the numerical character of the present analysis which is based on 0D models.

LES analysis

Five test cases are considered for LES analysis, in which hydrogen/methanol blend is varied between $\beta_X = 0.8$ and 1.0, c.f. Table 1, following the analyses in the previous section. The operating conditions and domain discretization are further described in Section LES configuration and test cases. In the following, spatio-temporal details of the TF ignition process are investigated.

Ignition delay time

Figure 8 depicts temporal evolution of the maximum temperature (T_{max}) in the domain, for each of the considered LES

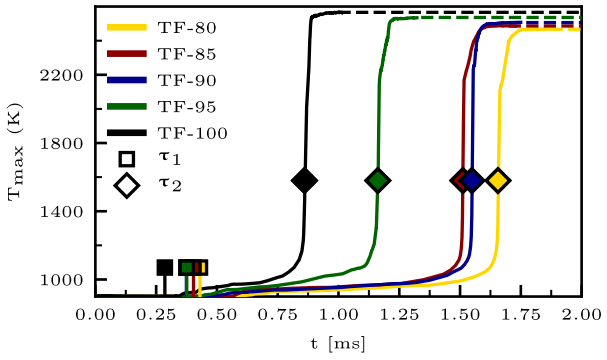

Fig. 8 – Temporal evolution of maximum temperature. First and second stage ignition delay time is advanced with more hydrogen, whereas ignition temperature is increased.

test cases. Square and diamond markers represent τ_1 and τ_2, respectively. Here, τ_1 is defined as the time instant when 20% of maximum RO_2 mass fraction is reached, while τ_2 is based on the maximum gradient of T_{max} in the system, i.e. $(dT_{max}/dt)_{max}$.

According to Fig. 8, both τ_1 and τ_2 are advanced with more hydrogen in the premixed charge, consistent with the findings in Ref. [40]. Additionally, the temperature of the products is noted to increase with more hydrogen, as indicated by dashed lines in the plots. Such a note is rather relevant to the higher adiabatic flame temperature and calorific value associated with hydrogen compared to methanol or diesel [8].

Regarding the second stage IDT, TF-95 and TF-100 show a significant τ_2 reduction (about 1.18 and 0.88 ms, respectively) compared with the other test cases ($\tau_2 \approx 1.55$ ms). This observation should be related to smaller hydrogen-to-methanol *mass* ratios in TF-80, TF-85 and TF-90 compared with TF-95 and TF-100, c.f. Fig. 2b. In particular, despite the wide β_X variations in the former three cases, β_Y variations are rather narrow. This is also reflected in the very close peak temperature values during the main ignition event in Fig. 8. The slightly reversed second-stage ignition timings in cases TF-85 and TF-90 could be related to the hyper-sensitivity of ignition delay time towards Z_{MR} in LES, which is further discussed in Section Heat release analysis. The mass blending ratio is doubled from $\beta_Y = 0.26$ in TF-85 to $\beta_Y = 0.54$ in TF-95 then to $\beta_Y = 1.0$ in TF-100. Therefore, in the remainder of this work we focus particularly on these cases to compare and analyze data with notable differences.

Spatial distribution of ignition stages

Figure 9 depicts the development of various stages of the ignition process for TF-85, TF-95, and TF-100 (left to right). Four time instances, linked with τ_1 and τ_2 time scales, are herein considered (top to bottom) which denote respectively i) τ_1, ii) $0.95\tau_2$ indicating HTC reactions onset, iii) τ_2 wherein second-stage ignition initiates with ignition kernels, and iv) $\tau_2 + 0.15$ ms representing a time instance with ignition front propagation through ambient. Here, dispersed liquid phase is represented by LPT point data (blue spheres), whereas translucent gray isosurfaces denote $Z_{st.}$. LTC and HTC stages are demonstrated by computational cells marking $Y_{RO_2} > 10^{-5}$ (green) and $T > 1600$ K (red), respectively, while the HTC spatial onset is herein depicted by H_2O_2 consumption rates ($\dot{\omega}_{H_2O_2} < 0$, cyan color).

According to the figure, the following observations are noted. At $t = \tau_1$, the onset and spatial distribution of LTC within the spray is presented. As noted earlier, more H_2 leads to a shorter τ_1. Therefore, an advance of approximately 0.1 ms in τ_1 from TF-85 to TF-100 leads to a 3–4 mm shifting of the LTC onset location as well as shortening the spray tip penetration length. Consequently, a tendency of LTC activation towards richer regions of the spray is attained with more H_2 in the premixed charge.

At $t = 0.95\tau_2$, slightly before high temperature ignition, spatial distribution of RO_2 products grows further downstream, and HTC reactions start to take place while LTC phase products are consumed. Such HTC onset locations denote most reactive zones of the spray in which high temperature ignition kernels are expected to initiate.

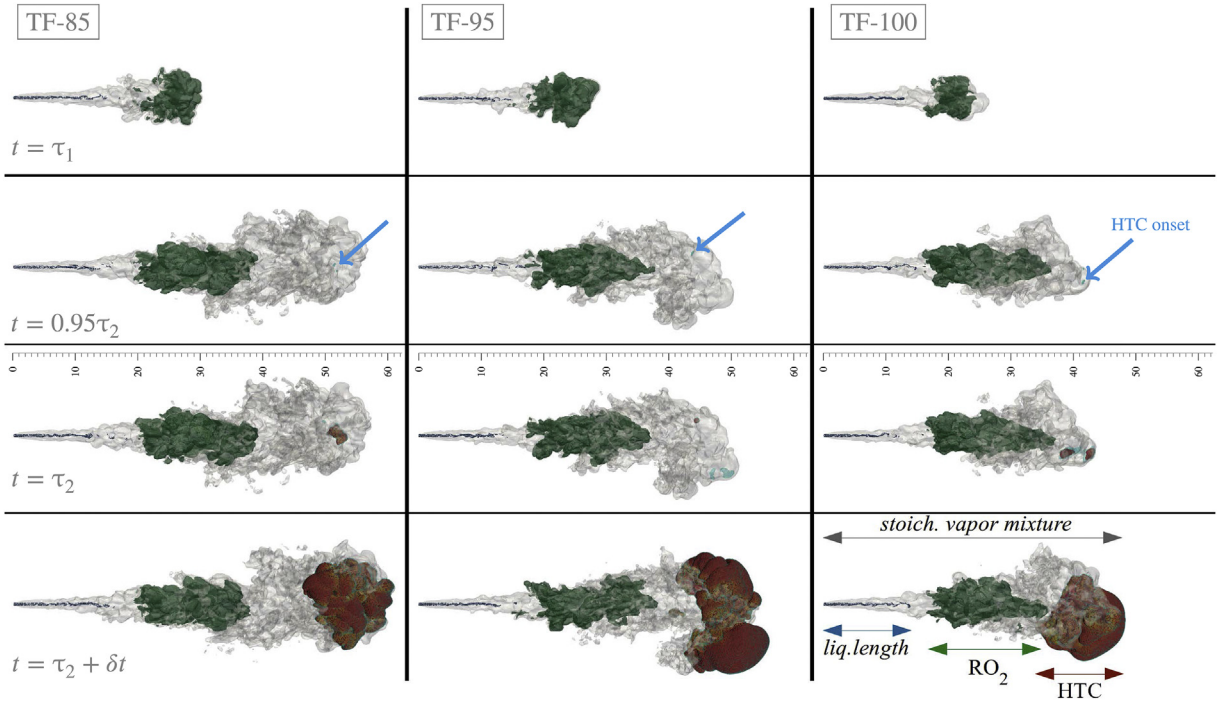

Fig. 9 – Spatio-temporal evolution of various stages of ignition process. Liquid spray and stoichiometric vapor mixture ($Z_{st.}$) are noted by LPT parcels (blue spheres) and translucent gray isosurfaces, respectively. LTC region (green) is marked by $RO_2 > 10^{-5}$ while HTC onset (cyan) is identified by $\dot{\omega}_{H_2O_2} < 0$. High temperature ignition kernels (red) are marked by $T > 1600$ K. (For interpretation of the references to color in this figure legend, the reader is referred to the Web version of this article.)

At $t = \tau_2$, the second-stage ignition takes place along with emerging high temperature kernels. These kernels are entirely located inside the spray, consistent with the spray assisted ignition concept, and closer to the spray periphery. Also, the overlapping of red and cyan colors demonstrates the breakup of H_2O_2 species at high temperatures, i.e. the HTC onset. In the TF-95 case, a new cyan region without overlapped red color indicates another HTC kernel to ignite soon, apart from the first ignited kernel.

Finally, at $t = \tau_2 + 0.15$ ms, the ignition front grows further across the spray and starts burning methanol and hydrogen in the ambient. A summary of quantitative findings from LES cases is provided in Table 3. Penetration lengths for liquid, i.e. L_{liq}, and vapor spray at τ_2, i.e. $L_{vap}(\tau_2)$, are defined by the maximal axial distance from the nozzle to where HRF liquid volume fraction and vaporized mass fraction, respectively, are 0.1%.

It should be noted that the present TF results are of numerical character. Certainly, experimental data would be rather substantial to complete the picture. However, the well-established numerical framework together with the validated kinetic mechanism (c.f. Appendix A) for the utilized fuels should be sufficient for the reliability of this study. Moreover, the inhibiting effects of methanol or hydrogen in DF ignition (c.f. Fig. 4 and Table 3 respectively), compared with SF diesel (IDT ≈ 0.39 ms [73]), can be related to experimental works in literature for DF methanol [12,13] and hydrogen [23,29].

Temporal evolution of key species

Temporal evolution of the mass fractions $Y_{RO_2}^{max}(--)$, $Y_{OH}^{max}(-)$, $Y_{H_2O_2}^{max}(--)$ and $Y_{HO_2}^{max}(-)$ are presented in Fig. 10 with color correspondence noted in the legend. With relevance to these important radicals and intermediate species, the following process is noted among all of the considered cases. First, within τ_1 time scale, low-temperature ignition occurs and RO_2 peak values are formed. Second, HO_2 radicals are formed during both first- and second-stage ignition phases, with more significance during the HTC phase. Third, H_2O_2 is formed by intermediate reactions. Since H_2O_2 is stable at low and intermediate temperatures, it does not break up prior to τ_2 after which it forms OH radicals [74].

According to Fig. 10, adding hydrogen has the following effects on species evolution. First, within τ_1 time scale, the formation of RO_2 is advanced with higher peak magnitudes. Moreover, both HO_2 and H_2O_2 formations are advanced with higher peak magnitudes during the entire LTC phase. Second, within τ_2 time scale, HO_2 and OH formations are advanced. However, an opposing trend between the mentioned species is observed, particularly higher peaks for OH and lower peaks for HO_2. This phenomenon can be related to higher temperature levels during the second stage ignition with more hydrogen, c.f. Fig. 8. It is expected that the production intensity of OH increases with temperature. In addition, higher temperatures can play a role in speeding up slow HO_2 reactions to produce H_2O_2 [40], hence the lower HO_2 concentration peaks in cases with more hydrogen.

Table 3 – Summary of quantitative results for the LES cases.

	τ_1 [ms]	τ_2 [ms]	τ_2/τ_1	τ_2/IDT_{MR}^{0d}	L_{liq} [mm]	$L_{vap}(\tau_2)$ [mm]
TF-80	0.43	1.66	3.85	2.875	14.15 ± 2.11	62.00
TF-85	0.40	1.51	3.78	2.753	14.08 ± 2.04	56.73
TF-90	0.37	1.55	4.19	2.997	14.03 ± 2.09	55.90
TF-95	0.36	1.16	3.22	2.430	13.90 ± 2.30	50.87
TF-100	0.286	0.86	3.01	2.003	13.80 ± 2.38	43.71

Heat release analysis

Here, further investigations with respect to heat release rate are provided. Fig. 11 presents HRR scatter plots within the spray envelope ($Z > 10^{-5}$) in Z space at the time scales τ_2 (upper row) and $\tau_2 + 0.15$ ms (bottom row). The plots are overlayed with HRR conditional means (—) and standard deviations (filled region). Also, IDT plots from 0D data (τ_2^{0d}, —) are provided which consider chemical kinetics without turbulent mixing effects.

According to Fig. 11 at τ_2, Z_{MR} values in LES data (i.e. HRR peaks corresponding to ignition kernels) are always on the richer side of $Z_{st.}$, following the spray assisted ignition concept in LES. Also, these peaks are located on the leaner side of Z_{MR} in 0D, due to the turbulent mixing time considered in the 3D data. Such an observation is consistent with those reported by Kahila et al. [6,34]. Moreover in TF-100, the two simultaneous ignition kernels occurred at τ_2, c.f. Fig. 9, are herein represented by two HRR peaks of varied mixture fraction values, due to the spray dilution while progressing away from the nozzle. Furthermore, it is observed that with H_2 addition, Z_{MR} in LES shifts to richer conditions and converges towards Z_{MR} in 0D, which is related to the shorter mixing time due to the shorter spray.

At $t = \tau_2 + 0.15$ ms, ignition fronts in all of the considered cases have burned ambient LRFs (methanol and hydrogen) across the spray, with a broader interval of burned mixture fractions in cases with more H_2. Finally, less hydrogen in the system shifts Z_{MR} values of 3D data towards a *hyper-sensitive* region of 0D IDT profile with a steep slope, wherein a small perturbation in Z leads to significant effects on IDT, hence questioning the ignition robustness and the potential of cyclic variations. This specific note can elaborate on the observed trend in T-85 and TF-90 cases wherein respective IDTs are located around this hyper-sensitive region. This situation improves with further hydrogen enrichment because Z_{MR} shifts to a more stable region in 0D IDT profiles which are less sensitive to Z perturbations.

Ignition mode decomposition

The following analysis, depicted in Fig. 12, considers identification of different ignition modes based on HRR, with relevance to LTC and HTC phases. Five ignition modes are herein considered, namely the (i) early LTC: wherein *n*-dodecane decomposition initiates, (ii) LTC: denoting the production of various LTC species, (iii) pre-HTC: in which RO_2 radicals are consumed during HTC transition, (iv) HTC pre-ignition: corresponding to the high temperature phase yet without OH formation, and (v) HTC: denoting full ignition with OH formation. The employed criteria for each ignition mode is described in Table 4 with threshold values similar to those in Ref. [34], and respective color correspondence as shown in the figure legend. While these ignition modes are defined within the spray ($Z > 10^{-4}$), temporal evolution (up until $\tau_2 + 0.15$ ms)

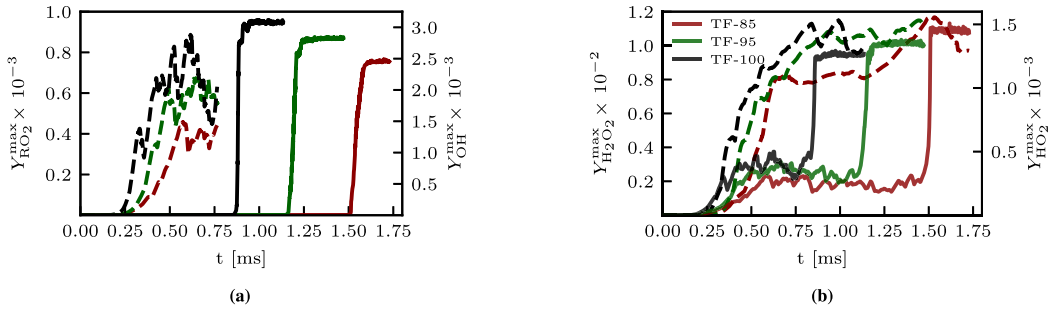

Fig. 10 – Temporal evolution of (a) Y_{RO_2}(- -), Y_{OH}(——) and (b) $Y_{H_2O_2}$(- -), Y_{HO_2}(——). It is noted that, within τ_1 adding hydrogen advances RO_2 production with higher peak magnitudes, and similarly HO_2 and H_2O_2 for the entire LTC duration. However, within τ_2 adding H_2 advances HO_2 with lower peaks and OH with higher peaks.

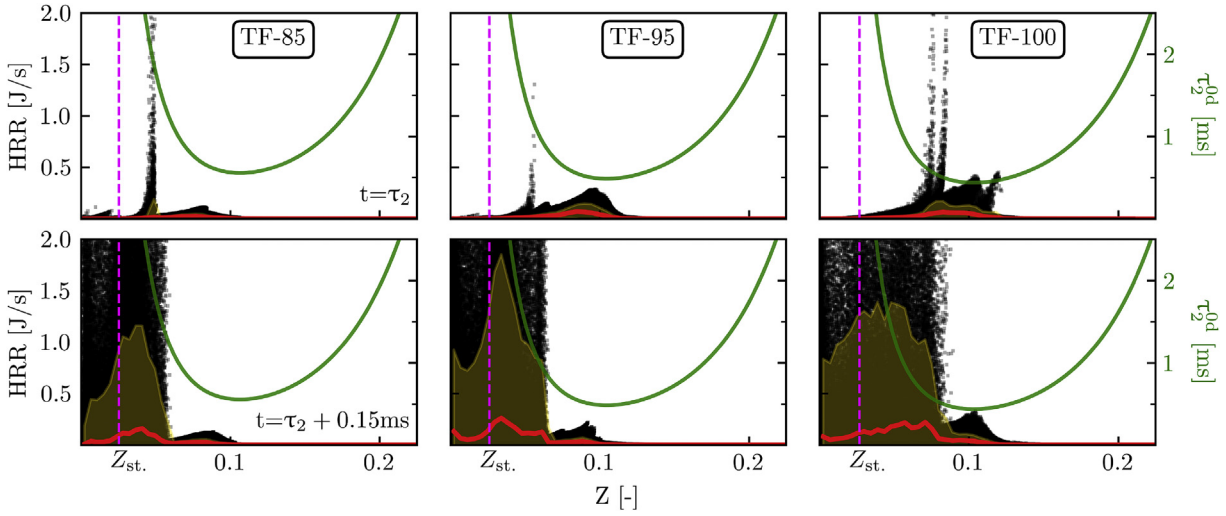

Fig. 11 – Scatter plots of HRR in Z space for the spray region, overlayed with conditional means (red) and standard deviation (filled) at times $t = \tau_2$ and $\tau_2 + 0.15$ ms, while green curves represent 0D IDT values. With H_2 addition, Z_{MR} shifts to richer conditions and converges towards Z_{MR} in 0D. Also, with relevance to 0D plots, IDT becomes less sensitive towards perturbations in Z_{MR} from LES, hence promoting ignition robustness. (For interpretation of the references to color in this figure legend, the reader is referred to the Web version of this article.)

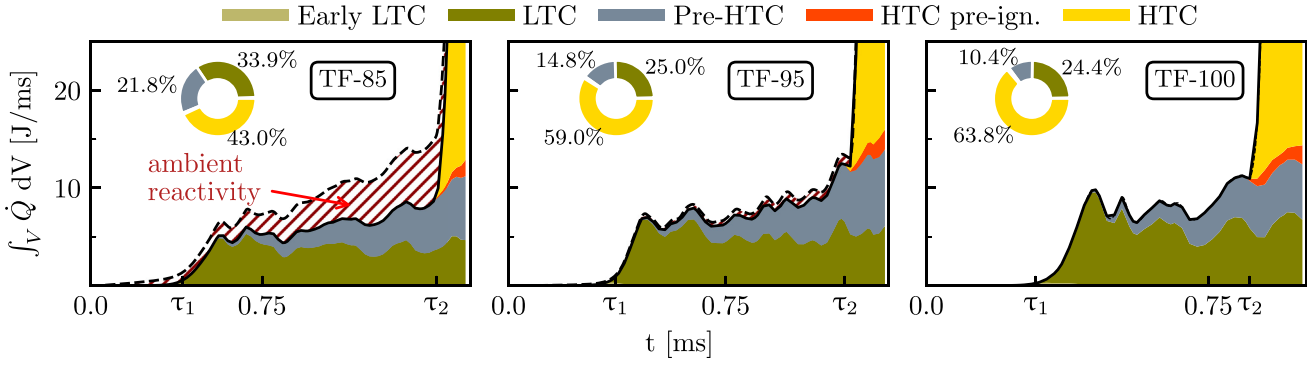

Fig. 12 – Ignition mode decomposition based on temporal evolution (till $\tau_2 + 0.15$ ms) of the heat release rates. (——) represents total heat release inside spray ($Z_{st} > 1e-4$) whereas (- - -) represents total heat release in the whole domain. Hatched region denotes ambient reactivity. Pie chart indicates cumulative percentage of each ignition mode. The figure shows that ambient reactivity persists for $\beta_X < 0.95$ after which it is mitigated and ambient autoignition becomes less probable.

Table 4 – Criteria for ignition modes. $RO2^{\star} = 10^{-5}$, $H2O2^{\star} = 10^{-4}$, $OH^{\star} = 10^{-5}$, $T^{\star} = 1150$ K.

Mode	Definition
Early LTC	$(RO2 \geq 10^{-7}) \cap (H2O2 < H2O2^{\star}) \cap (T < T^{\star})$
LTC	$(RO2 \geq RO2^{\star}) \cap (H2O2 \geq H2O2^{\star}) \cap (T < T^{\star})$
Pre-HTC	$(RO2 < RO2^{\star}) \cap (H2O2 \geq H2O2^{\star}) \cap (T < T^{\star})$
HTC pre-ign.	$(OH < OH^{\star}) \cap (T \geq T^{\star})$
HTC	$(OH \geq OH^{\star}) \cap (T \geq T^{\star})$

of total heat release rate (THRR) for the whole domain is also plotted (▪ ▪ ▪). Generally, a typical DF or TF setup results in THRR that is generated entirely inside the spray, i.e. a non-reactive ambient, prior to τ_2.

According to Fig. 12, in TF-85, the observed HRR outside the spray periphery ($Z < 10^{-4}$, hatched region) along the entire time interval denotes ambient reactivity, which suggests a higher possibility to the unfavorable ambient autoignition. In this case, the relatively large methanol content in the ambient (here, 79.9% by mass compared with 20.1% hydrogen) can explain this behavior due to its higher reactivity at higher temperatures. This is aligned with literature noting the possibility of methanol utilization as HRF in CI engines [75], or its auto-ignition potential in the ambient [76]. However, with more H_2 in TF-95 and TF-100, the THRR (▪ ▪ ▪) and spray's THRR (▬) overlay, i.e. the ambient autoignition becomes less probable. This is related to lower reactivity of hydrogen compared with methanol, c.f. Fig. 5. Therefore, according to this analysis, more than 50% of H_2 blending mass percentage (about 94% molar) is needed to achieve smooth TF ignition, under the specified ambient conditions. Further demonstrations on the ambient reactivity are provided in Appendix C.

Besides previous notes in Fig. 12, the following observations are noted. First, spray's HTC share to THRR is larger with more H_2. Considering the fixed interval of 0.15 ms beyond τ_2, this larger share can be attributed to higher ignition temperature and faster flame propagation of H_2 compared with CH_3OH. Second, with more H_2 the spray's LTC contribution to THRR increases, consistent with observations in Fig. 10 for RO_2 peaks. However, a cumulative LTC percentage declines with more H_2 due to the increased HTC contribution in the normalized pie-chart. Finally, it is noted that the HTC pre-ignition mode initiates slightly before the HTC mode (similarly early LTC before LTC mode) with a relatively insignificant contribution. Such a minimal contribution in the HTC pre-ignition is attributed to steep gradients of temperature and OH profiles during the second-stage ignition, c.f. Fig. 8 and. The HTC pre-ignition mode contribution becomes significantly stronger in less reactive fuels with less steep ignition profiles, such as methane as demonstrated in Refs. [34,43].

Conclusions and perspectives

Large-eddy simulation (LES), Lagrangian particle tracking (LPT) and finite-rate chemistry were successively employed to investigate the characteristics associated with tri-fuel (TF) ignition system. A pilot *n*-dodecane spray was used as a high reactivity fuel (HRF) to ignite homogeneously premixed lean charge comprising oxidizer, EGR, and a blend of two low reactivity fuels (LRFs): methanol (CH_3OH) and hydrogen (H_2). The injection and ambient thermodynamic conditions were similar to the ECN Spray A. Prior to LES, a set of zero-dimensional (0D) homogeneous reactor simulations was performed, with the aim of providing insight towards the mixture's ignitability at a broad range of operating conditions involving T_{amb}, ϕ_{amb}, and hydrogen-to-methanol blending ratio β. Based on that, five computationally expensive simulations were performed at targeted conditions for $0.8 \leq \beta_X \leq 1.0$.

The main findings of the present study can be summarized as follows. First, the multi-parametric 0D analyses reveal that the narrow smooth ignition window of *n*-dodecane/CH_3OH DF mixture can be extended via H_2 enrichment (see e.g. Fig. 7). Second, based on LES analysis, doubling the H_2 blending mass ratio (25%–50% or 50%–100%) in the premixed charge could potentially advance IDT by 23–26%, with shorter penetrations (10–15%) of the vaporized spray. Third, with H_2 addition the most reactive zones occur at richer mixtures due to faster chemistry, and the ignition front propagates by spanning a broader range of mixture fractions. More importantly, a cross comparison with 0D IDTs suggests that large H_2 blending ratios (about 94% molar, 50% by mass) promotes ignition robustness, hence a less probability to cycle-to-cycle combustion variation in real engine conditions. Fourth, ambient reactivity persists in the studied system at lower H_2 concentrations, which might raise concerns regarding abnormal ignition. More than 50% of H_2 mass ratio is required to ensure a non-reactive ambient. Fifth, with respect to ignition modes, adding H_2 increases both low- and high-temperature combustion shares in a spray's total HRR. Finally, we acknowledge the numerical character of the present study, and that dynamic phenomena, such as engine speed and dynamic compression, were herein neglected for computational feasibility. Therefore, it would be of high importance to gain experimental data on tri-fuel combustion of methanol and hydrogen blends.

CRediT authorship contribution statement

Mahmoud Gadalla: Conceptualization, Methodology, Software, Visualization, Writing - Original Draft. **Jeevananthan Kannan:** Methodology, Investigation, Writing - Original Draft. **Bulut Tekgül:** Methodology, Software, Validation, Writing - Original Draft. **Shervin Karimkashi:** Validation, Writing - Review & Editing, Supervision. **Ossi Kaario:** Conceptualization, Writing - Review & Editing, Supervision. **Ville Vuorinen:** Conceptualization, Writing - Review & Editing, Supervision, Funding acquisition.

Declaration of competing interest

The authors declare that they have no known competing financial interests or personal relationships that could have appeared to influence the work reported in this paper.

Acknowledgements

The present study has been financially supported by the Academy of Finland [grant numbers 318024 and 332784]. The first author acknowledges financial support from Merenkulun säätiö. Computational resources were provided by CSC — Finnish IT Center for Science.

Appendix A. Chemical mechanism validation and comparison

The employed POLIMI-96 chemical kinetic mechanism, which is developed for *n*-dodecane oxidation under engine-relevant conditions, is herein validated against single fuel experimental data for methanol (Burke et al. [77]) and hydrogen (Kéromnès et al. [78]) oxidation. Figure A.1 presents IDT values at various temperatures for a homogeneous mixture corresponding to $\phi = 0.5$ and pressure of 50 bar (methanol) and 1 bar or 16 bar (hydrogen). The validation data for methanol are also compared with simulations using some mechanisms developed specifically for methanol by Klippenstein [71] and Lindstedt [79]. Further validations can be found in the works by Karimkashi et al. [40,60].

In addition, ignition delay time sensitivity against kinetic chemical mechanism choice is herein presented. A homogeneous mixture comprising oxidizer, EGR, CH_3OH and H_2, with LRFs molar blending ratio $\beta_X = 0.5$ and $\phi_{amb} = 0.5$ is prepared. Figure A.2 depicts IDT predictions of the mentioned mixture at varied ambient temperatures.

A set of common mechanisms involving CH_3OH and H_2 reaction pathways is considered for comparison. Besides Klippenstein et al. [71], the skeletal *n*-dodecane mechanism by Wang et al. [80] (100 species and 432 reactions) and the detailed mechanism by Bagheri et al. [81] (namely POLIMI-detailed, with 492 species and 17,790 reactions) are tested. Also, reduced (163 species and 887 reactions) and detailed (2885 species and 11,754 reactions) versions of the *n*-dodecane mechanism developed by Lawrence Livermore National Laboratory (LLNL) [82] are considered. The plots show that POLIMI-96 mechanism is in proper agreement with the mentioned mechanisms.

By adding HRF to the mixture for a specific ambient temperature (here 1000 K) and varied mixture fraction, significant differences are noted as depicted in Figure A.2b. Particularly, closer to stoichiometric mixture fraction an inflection behavior is observed for some mechanisms which are POLIMI-96 and a skeletal *n*-heptane mechanism by Lu et al. [83], whereas mild inflections in POLIMI-detailed and LLNL-detailed are noted. Remaining mechanisms are observed to maintain conventional parabolic patterns, i.e. without inflections, along the mixing line.

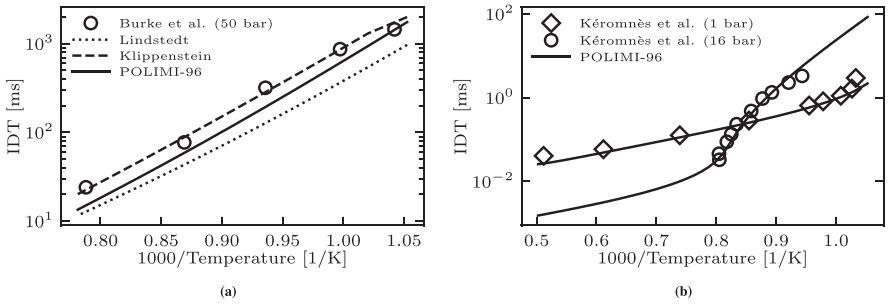

Figure A.1: Chemical mechanism validation for the oxidation of (a) methanol, and (b) hydrogen against experimental data for $\phi = 0.5$ and pressure values as indicated in the figure legend.

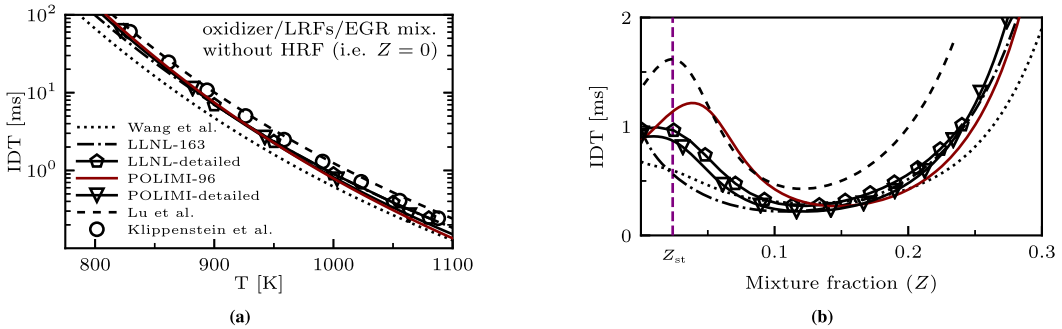

Figure A.2: Chemical mechanism comparison for IDT predictions of oxidizer/LRFs/EGR (a) without HRF ($Z = 0$) at varied T_{amb}, and (b) with HRF at varied Z. The employed POLIMI-96 is in proper agreement with most of common mechanisms for similar conditions, however the observed inflection seems to be sensitive to the mechanism choice.

B. Mesh sensitivity

Another computational grid with a finer resolution is considered here for mesh sensitivity analysis. This new grid holds a total of 39 M cells with 62.5 μm grid spacing in the inner most refinement layer. A comparison of standard (utilized throughout the paper) and fine grid resolutions is shown in Figure B.1a, and a new reacting LES for the TF-100 case is performed using this fine grid. The temporal evolution of T^{max} (black) and $Y_{RO_2}^{max}$ (green) are depicted in Figure B.1b. It is observed that the ignition delay is rather insensitive to the employed mesh resolution for the mentioned case, while the computational load (in terms of CPU-hours) was increased by a factor of approximately 20 for simulating 1.0 ms compared to the same case utilizing a standard mesh.

C. Ambient reactivity demonstration

The ambient reactivity, previously discussed in Section Ignition mode decomposition, is herein further demonstrated. Figure C.1a depicts temporal evolution of the THRR conditioned with Z. The plot shows that ambient reactivity occurs as early as τ_1 time scale and it increases with time progress. In Figure C.1b, comparative representation of THRR for TF-80 against non-reactive ambient cases shows ambient reactivity effects on disturbing the observed trends within τ_1 phase (i.e. monotonic reduction of the HRR peaks with less H_2 for non-reactive ambient TF cases) as well as chemical induction phase.

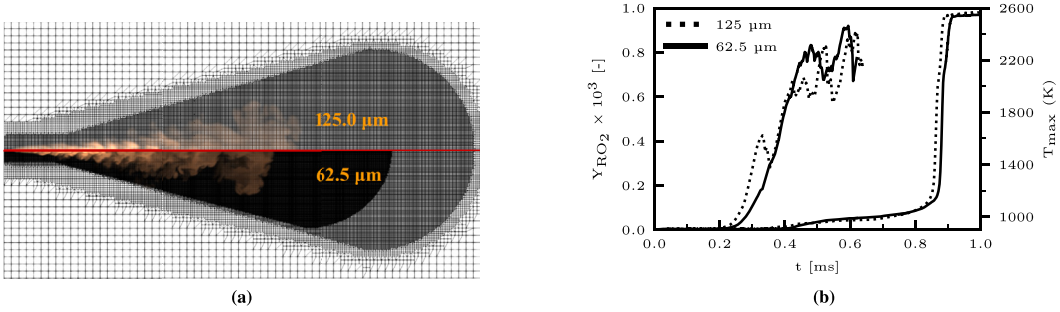

Figure B.1: (a) Mesh comparison between standard (125 μm) and fine (62.5 μm) resolutions of the discretized spray region. (b) Temporal evolution of T_{amb}^{max} (black) and $Y_{RO_2}^{max}$ (green) for TF-100 case using a standard or fine grid. The plot shows that IDT seems to be rather insensitive to the employed standard mesh resolution in the mentioned case.

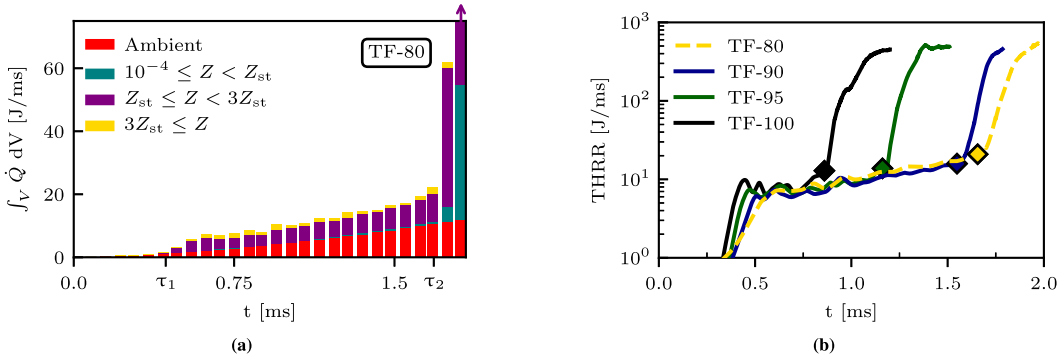

Figure C.1: Demonstration of the ambient reactivity in the case TF-80 with relevance to (a) Z distribution, and (b) THRR compared with other TF cases.

REFERENCES

[1] Muradov N, Veziroglu T. "green" path from fossil-based to hydrogen economy: an overview of carbon-neutral technologies. Int J Hydrogen Energy 2008;33(23):6804–39. https://doi.org/10.1016/j.ijhydene.2008.08.054.

[2] Wall TF. Combustion processes for carbon capture. Proc Combust Inst 2007;31(1):31–47. https://doi.org/10.1016/j.proci.2006.08.123.

[3] Chen W-H, Lin B-J. Hydrogen and synthesis gas production from activated carbon and steam via reusing carbon dioxide. Appl Energy 2013;101:551–9. https://doi.org/10.1016/j.apenergy.2012.06.030.

[4] Reitz RD, Duraisamy G. Review of high efficiency and clean reactivity controlled compression ignition (RCCI) combustion in internal combustion engines. Prog Energy Combust Sci 2015;46:12–71. https://doi.org/10.1016/j.pecs.2014.05.003.

[5] Papagiannakis R, Hountalas D. Combustion and exhaust emission characteristics of a dual fuel compression ignition engine operated with pilot diesel fuel and natural gas. Energy Convers Manag 2004;45(18–19):2971–87. https://doi.org/10.1016/j.enconman.2004.01.013.

[6] Kahila H, Wehrfritz A, Kaario O, Vuorinen V. Large-eddy simulation of dual-fuel ignition: diesel spray injection into a lean methane-air mixture. Combust Flame 2019;199:131–51. https://doi.org/10.1016/j.combustflame.2018.10.014.

[7] Kannan J, Gadalla M, Tekgül B, Karimkashi S, Kaario O, Vuorinen V. Large eddy simulation of diesel spray–assisted dual-fuel ignition: a comparative study on two n-dodecane mechanisms at different ambient temperatures. Int J Engine Res 2020. https://doi.org/10.1177/1468087420946551. 146808742094655.

[8] Verhelst S, Turner JW, Sileghem L, Vancoillie J. Methanol as a fuel for internal combustion engines. Prog Energy Combust Sci 2019;70:43–88. https://doi.org/10.1016/j.pecs.2018.10.001.

[9] Chintala V, Subramanian K. Assessment of maximum available work of a hydrogen fueled compression ignition engine using exergy analysis. Energy 2014;67:162–75. https://doi.org/10.1016/j.energy.2014.01.094.

[10] Izbassarov D, Nyári J, Tekgül B, Laurila E, Kallio T, Santasalo-Aarnio A, Kaario O, Vuorinen V. A numerical performance study of a fixed-bed reactor for methanol synthesis by CO2 hydrogenation. Int J Hydrogen Energy Mar. 2021;46:15635–48. https://doi.org/10.1016/j.ijhydene.2021.02.031.

[11] Pedersen-Mjaanes H, Chan L, Mastorakos E. Hydrogen production from rich combustion in porous media. Int J Hydrogen Energy 2005;30(6):579–92. https://doi.org/10.1016/j.ijhydene.2004.05.006.

[12] Duraisamy G, Rangasamy M, Govindan N. A comparative study on methanol/diesel and methanol/PODE dual fuel RCCI combustion in an automotive diesel engine. Renew Energy 2020;145:542–56. https://doi.org/10.1016/j.renene.2019.06.044.

[13] Wei L, Yao C, Han G, Pan W. Effects of methanol to diesel ratio and diesel injection timing on combustion, performance and emissions of a methanol port premixed diesel engine. Energy 2016;95:223–32. https://doi.org/10.1016/j.energy.2015.12.020.

[14] Wang Q, Wei L, Pan W, Yao C. Investigation of operating range in a methanol fumigated diesel engine. Fuel 2015;140:164–70. https://doi.org/10.1016/j.fuel.2014.09.067.

[15] Wu T, Yao A, Yao C, Pan W, Wei H, Chen C, Gao J. Effect of diesel late-injection on combustion and emissions characteristics of diesel/methanol dual fuel engine. Fuel 2018;233:317–27. https://doi.org/10.1016/j.fuel.2018.06.063.

[16] Duraisamy G, Rangasamy M, Nagarajan G. Effect of EGR and premixed mass percentage on cycle to cycle variation of methanol/diesel dual fuel RCCI combustion. In: SAE technical paper series, SAE international; 2019. https://doi.org/10.4271/2019-26-0090.

[17] Wang Q, Wang B, Yao C, Liu M, Wu T, Wei H, Dou Z. Study on cyclic variability of dual fuel combustion in a methanol fumigated diesel engine. Fuel 2016;164:99–109. https://doi.org/10.1016/j.fuel.2015.10.003.

[18] Li Y, Jia M, Liu Y, Xie M. Numerical study on the combustion and emission characteristics of a methanol/diesel reactivity controlled compression ignition (RCCI) engine. Appl Energy 2013;106:184–97. https://doi.org/10.1016/j.apenergy.2013.01.058.

[19] Castro N, Toledo M, Amador G. An experimental investigation of the performance and emissions of a hydrogen-diesel dual fuel compression ignition internal combustion engine. Appl Therm Eng 2019;156:660–7. https://doi.org/10.1016/j.applthermaleng.2019.04.078.

[20] Nag S, Sharma P, Gupta A, Dhar A. Experimental study of engine performance and emissions for hydrogen diesel dual fuel engine with exhaust gas recirculation. Int J Hydrogen Energy 2019;44(23):12163–75. https://doi.org/10.1016/j.ijhydene.2019.03.120.

[21] Dimitriou P, Kumar M, Tsujimura T, Suzuki Y. Combustion and emission characteristics of a hydrogen-diesel dual-fuel engine. Int J Hydrogen Energy 2018;43(29):13605–17. https://doi.org/10.1016/j.ijhydene.2018.05.062.

[22] Talibi M, Hellier P, Ladommatos N. The effect of varying EGR and intake air boost on hydrogen-diesel co-combustion in CI engines. Int J Hydrogen Energy 2017;42(9):6369–83. https://doi.org/10.1016/j.ijhydene.2016.11.207.

[23] Gnanamoorthi V, Vimalananth V. Effect of hydrogen fuel at higher flow rate under dual fuel mode in CRDI diesel engine. Int J Hydrogen Energy 2020;45(33):16874–89. https://doi.org/10.1016/j.ijhydene.2020.04.145.

[24] Liu X, Srna A, Yip HL, Kook S, Chan QN, Hawkes ER. Performance and emissions of hydrogen-diesel dual direct injection (h2ddi) in a single-cylinder compression-ignition engine. Int J Hydrogen Energy 2021;46(1):1302–14. https://doi.org/10.1016/j.ijhydene.2020.10.006.

[25] Hosseini SM, Ahmadi R. Performance and emissions characteristics in the combustion of co-fuel diesel-hydrogen in a heavy duty engine. Appl Energy 2017;205:911–25. https://doi.org/10.1016/j.apenergy.2017.08.044.

[26] Ahmadi R, Hosseini SM. Numerical investigation on adding/substituting hydrogen in the CDC and RCCI combustion in a heavy duty engine. Appl Energy 2018;213:450–68. https://doi.org/10.1016/j.apenergy.2018.01.048.

[27] Jabbr AI, Koylu UO. Influence of operating parameters on performance and emissions for a compression-ignition engine fueled by hydrogen/diesel mixtures. Int J Hydrogen Energy 2019;44(26):13964–73. https://doi.org/10.1016/j.ijhydene.2019.03.201.

[28] Yuan C, Han C, Liu Y, He Y, Shao Y, Jian X. Effect of hydrogen addition on the combustion and emission of a diesel free-piston engine. Int J Hydrogen Energy 2018;43(29):13583–93. https://doi.org/10.1016/j.ijhydene.2018.05.038.

[29] Kumar CB, Lata D, Mahto D. Analysis of ignition delay by taking di-tertiary-butyl peroxide as an additive in a dual fuel diesel engine using hydrogen as a secondary fuel. Int J Hydrogen Energy 2020;45(29):14806–20. https://doi.org/10.1016/j.ijhydene.2020.03.212.

[30] Lata D, Misra A. Analysis of ignition delay period of a dual fuel diesel engine with hydrogen and LPG as secondary fuels. Int J Hydrogen Energy 2011;36(5):3746–56. https://doi.org/10.1016/j.ijhydene.2010.12.075.

[31] Akal D, Öztuna S, Büyükakın MK. A review of hydrogen usage in internal combustion engines (gasoline-lpg-diesel) from combustion performance aspect. Int J Hydrogen Energy

2020;45(60):35257–68. https://doi.org/10.1016/j.ijhydene.2020.02.001.
[32] Menaa A, Lounici M, Amrouche F, Loubar K, Kessal M. CFD analysis of hydrogen injection pressure and valve profile law effects on backfire and pre-ignition phenomena in hydrogen-diesel dual fuel engine. Int J Hydrogen Energy 2019;44(18):9408–22. https://doi.org/10.1016/j.ijhydene.2019.02.123.
[33] Tekgül B, Kahila H, Kaario O, Vuorinen V. Large-eddy simulation of dual-fuel spray ignition at different ambient temperatures. Combust Flame 2020;215:51–65. https://doi.org/10.1016/j.combustflame.2020.01.017.
[34] Kahila H, Kaario O, Ahmad Z, Masouleh MG, Tekgül B, Larmi M, Vuorinen V. A large-eddy simulation study on the influence of diesel pilot spray quantity on methane-air flame initiation. Combust Flame 2019;206:506–21. https://doi.org/10.1016/j.combustflame.2019.05.025.
[35] Li Y, Li H, Guo H, Li Y, Yao M. A numerical investigation on methane combustion and emissions from a natural gas-diesel dual fuel engine using CFD model. Appl Energy 2017;205:153–62. https://doi.org/10.1016/j.apenergy.2017.07.071.
[36] Boushaki T, Dhué Y, Selle L, Ferret B, Poinsot T. Effects of hydrogen and steam addition on laminar burning velocity of methane–air premixed flame: experimental and numerical analysis. Int J Hydrogen Energy 2012;37(11):9412–22. https://doi.org/10.1016/j.ijhydene.2012.03.037.
[37] Li Y, Jia M, Xu L, Bai X-S. Multiple-objective optimization of methanol/diesel dual-fuel engine at low loads: a comparison of reactivity controlled compression ignition (RCCI) and direct dual fuel stratification (DDFS) strategies. Fuel 2020;262:116673. https://doi.org/10.1016/j.fuel.2019.116673.
[38] Wang B, Yao A, Yao C, Chen C, Lu H, Feng J. Experimental investigation on methanol auto-ignition in a compression ignition engine under DMDF mode. Fuel 2019;237:133–41. https://doi.org/10.1016/j.fuel.2018.09.154.
[39] Verhelst S. Recent progress in the use of hydrogen as a fuel for internal combustion engines. Int J Hydrogen Energy 2014;39(2):1071–85. https://doi.org/10.1016/j.ijhydene.2013.10.102.
[40] Karimkashi S, Kahila H, Kaario O, Larmi M, Vuorinen V. Numerical study on tri-fuel combustion: ignition properties of hydrogen-enriched methane-diesel and methanol-diesel mixtures. Int J Hydrogen Energy Jan. 2020;45:4946–62. https://doi.org/10.1016/j.ijhydene.2019.12.033.
[41] Ouchikh S, Lounici M, Tarabet L, Loubar K, Tazerout M. Effect of natural gas enrichment with hydrogen on combustion characteristics of a dual fuel diesel engine. Int J Hydrogen Energy 2019;44(26):13974–87. https://doi.org/10.1016/j.ijhydene.2019.03.179.
[42] Taghavifar H, Khalilarya S, Mirhasani S, Jafarmadar S. Numerical energetic and exergetic analysis of CI diesel engine performance for different fuels of hydrogen, dimethyl ether, and diesel under various engine speeds. Int J Hydrogen Energy 2014;39(17):9515–26. https://doi.org/10.1016/j.ijhydene.2014.03.256.
[43] Kannan J, Gadalla M, Tekgül B, Karimkashi S, Kaario O, Vuorinen V. Large-eddy simulation of tri-fuel ignition: diesel spray-assisted ignition of lean hydrogen–methane–air mixtures. Combust Theor Model 2021:1–24. https://doi.org/10.1080/13647830.2021.1887525.
[44] Gadalla M, Kannan J, Tekgül B, Karimkashi S, Kaario O, Vuorinen V. Large-eddy simulation of ECN spray A: sensitivity study on modeling assumptions. Energies 2020;13(13):3360. https://doi.org/10.3390/en13133360.
[45] Wehrfritz A, Vuorinen V, Kaario O, Larmi M. Large eddy simulation of high-velocity fuel sprays: studying mesh resolution and breakup model effects for spray A. Atomization Sprays 2013;23(5):419–42. https://doi.org/10.1615/atomizspr.2013007342.
[46] Tekgül B, Kahila H, Karimkashi S, Kaario O, Ahmad Z, Lendormy É, Hyvönen J, Vuorinen V. Large-eddy simulation of spray assisted dual-fuel ignition under reactivity-controlled dynamic conditions. Fuel 2021;293:120295. https://doi.org/10.1016/j.fuel.2021.120295.
[47] Poinsot T, Veynante D. Theoretical and numerical combustion. 2011.
[48] Weller HG, Tabor G, Jasak H, Fureby C. A tensorial approach to computational continuum mechanics using object-oriented techniques. Comput Phys 1998;12(6):620. https://doi.org/10.1063/1.168744.
[49] Issa R, Ahmadi-Befrui B, Beshay K, Gosman A. Solution of the implicitly discretised reacting flow equations by operator-splitting. J Comput Phys 1991;93(2):388–410. https://doi.org/10.1016/0021-9991(91)90191-m.
[50] Jasak H, Weller H, Gosman A. High resolution NVD differencing scheme for arbitrarily unstructured meshes. Int J Numer Methods Fluid 1999;31(2):431–49. https://doi.org/10.1002/(sici)1097-0363(19990930)31:2<431::aid-fld884>3.0.co;2-t.
[51] Kahila H, Wehrfritz A, Kaario O, Masouleh MG, Maes N, Somers B, Vuorinen V. Large-eddy simulation on the influence of injection pressure in reacting spray A. Combust Flame 2018;191:142–59. https://doi.org/10.1016/j.combustflame.2018.01.004.
[52] Laitinen A, Saari K, Kukko K, Peltonen P, Laurila E, Partanen J, Vuorinen V. A computational fluid dynamics study by conjugate heat transfer in OpenFOAM: a liquid cooling concept for high power electronics. Int J Heat Fluid Flow 2020;85:108654. https://doi.org/10.1016/j.ijheatfluidflow.2020.108654.
[53] Peltonen P, Saari K, Kukko K, Vuorinen V, Partanen J. Large-eddy simulation of local heat transfer in plate and pin fin heat exchangers confined in a pipe flow. Int J Heat Mass Tran 2019;134:641–55. https://doi.org/10.1016/j.ijheatmasstransfer.2019.01.046.
[54] Laurila E, Koivisto S, Kankkunen A, Saari K, Maakala V, Järvinen M, Vuorinen V. Computational and experimental investigation of a swirl nozzle for viscous fluids. Int J Multiphas Flow 2020;128:103278. https://doi.org/10.1016/j.ijmultiphaseflow.2020.103278.
[55] Laurila E, Roenby J, Maakala V, Peltonen P, Kahila H, Vuorinen V. Analysis of viscous fluid flow in a pressure-swirl atomizer using large-eddy simulation. Int J Multiphas Flow 2019;113:371–88. https://doi.org/10.1016/j.ijmultiphaseflow.2018.10.008.
[56] Alessandro D, Stankovic I, Merci B. LES study of a turbulent spray jet: mesh sensitivity, mesh-parcels interaction and injection methodology. Flow, Turbul Combust 2019;103(2):537–64. https://doi.org/10.1007/s10494-019-00039-7.
[57] Vuorinen V, Hillamo H, Kaario O, Larmi M, Fuchs L. Large eddy simulation of droplet Stokes number effects on turbulent spray shape. Atomization Sprays 2010;20(2):93–114. https://doi.org/10.1615/atomizspr.v20.i2.10.
[58] Niemeyer KE, Curtis NJ, Sung C-J. pyJac: analytical jacobian generator for chemical kinetics. Comput Phys Commun 2017;215:188–203. https://doi.org/10.1016/j.cpc.2017.02.004.
[59] Frassoldati A, D'Errico G, Lucchini T, Stagni A, Cuoci A, Faravelli T, Onorati A, Ranzi E. Reduced kinetic mechanisms of diesel fuel surrogate for engine CFD simulations. Combust Flame 2015;162(10):3991–4007. https://doi.org/10.1016/j.combustflame.2015.07.039.
[60] Karimkashi S, Kahila H, Kaario O, Larmi M, Vuorinen V. A numerical study on combustion mode characterization for

locally stratified dual-fuel mixtures. Combust Flame 2020;214:121–35. https://doi.org/10.1016/j.combustflame.2019.12.030.
[61] Pei Y, Som S, Pomraning E, Senecal PK, Skeen SA, Manin J, Pickett LM. Large eddy simulation of a reacting spray flame with multiple realizations under compression ignition engine conditions. Combust Flame 2015;162(12):4442–55. https://doi.org/10.1016/j.combustflame.2015.08.010.
[62] Li Z, Cuoci A, Parente A. Large eddy simulation of MILD combustion using finite rate chemistry: effect of combustion sub-grid closure. Proc Combust Inst 2019;37(4):4519–29. https://doi.org/10.1016/j.proci.2018.09.033.
[63] Duwig C, Nogenmyr K-J, ki Chan C, Dunn MJ. Large eddy simulations of a piloted lean premix jet flame using finite-rate chemistry. Combust Theor Model 2011;15(4):537–68. https://doi.org/10.1080/13647830.2010.548531.
[64] Fureby C. Comparison of flamelet and finite rate chemistry LES for premixed turbulent combustion. In: 45th AIAA aerospace sciences meeting and exhibit. American Institute of Aeronautics and Astronautics; 2007. https://doi.org/10.2514/6.2007-1413.
[65] Varna A, Wehrfritz A, Hawkes ER, Cleary MJ, Lucchini T, D'Errico G, Kook S, Chan QN. Application of a multiple mapping conditioning mixing model to ECN spray A. Proc Combust Inst 2019;37(3):3263–70. https://doi.org/10.1016/j.proci.2018.06.007.
[66] Goodwin DG, Speth RL, Moffat HK, Weber BW. Cantera: an object-oriented software toolkit for chemical kinetics, thermodynamics, and transport processes. 2018. https://doi.org/10.5281/zenodo.1174508. version 2.4.0, https://www.cantera.org.
[67] Bilger R, Stårner S, Kee R. On reduced mechanisms for methane-air combustion in nonpremixed flames. Combust Flame 1990;80(2):135–49. https://doi.org/10.1016/0010-2180(90)90122-8.
[68] Mastorakos E. Ignition of turbulent non-premixed flames. Prog Energy Combust Sci 2009;35(1):57–97. https://doi.org/10.1016/j.pecs.2008.07.002.
[69] Siebers DL. Liquid-phase fuel penetration in diesel sprays. In: SAE technical paper series. SAE International; 1998. https://doi.org/10.4271/980809.
[70] Petersen EL, Kalitan DM, Simmons S, Bourque G, Curran HJ, Simmie JM. Methane/propane oxidation at high pressures: experimental and detailed chemical kinetic modeling. Proc Combust Inst 2007;31(1):447–54. https://doi.org/10.1016/j.proci.2006.08.034.
[71] Klippenstein SJ, Harding LB, Davis MJ, Tomlin AS, Skodje RT. Uncertainty driven theoretical kinetics studies for CH3OH ignition: HO2+CH3OH and O2+CH3OH. Proc Combust Inst 2011;33(1):351–7. https://doi.org/10.1016/j.proci.2010.05.066.
[72] Shamun S, Haşimoğlu C, Murcak A, Andersson Öivind, Tunér M, Tunestål P. Experimental investigation of methanol compression ignition in a high compression ratio HD engine using a box-behnken design. Fuel 2017;209:624–33. https://doi.org/10.1016/j.fuel.2017.08.039.
[73] Benajes J, Payri R, Bardi M, Martí-Aldaraví P. Experimental characterization of diesel ignition and lift-off length using a single-hole ECN injector. Appl Therm Eng 2013;58(1–2):554–63. https://doi.org/10.1016/j.applthermaleng.2013.04.044.
[74] Cain T. Autoignition of hydrogen at high pressure. Combust Flame 1997;111(1–2):124–32. https://doi.org/10.1016/s0010-2180(97)00005-9.
[75] Pucilowski M, Jangi M, Shamun S, Li C, Tuner M, Bai X-S. Effect of start of injection on the combustion characteristics in a heavy-duty DICI engine running on methanol. In: SAE technical paper series, SAE international; 2017. https://doi.org/10.4271/2017-01-0560.
[76] Zhen X, Liu D, Wang Y. The knock study of methanol fuel based on multi-dimensional simulation analysis. Energy 2017;122:552–9. https://doi.org/10.1016/j.energy.2017.01.106.
[77] Burke U, Metcalfe WK, Burke SM, Heufer KA, Dagaut P, Curran HJ. A detailed chemical kinetic modeling, ignition delay time and jet-stirred reactor study of methanol oxidation. Combust Flame 2016;165:125–36. https://doi.org/10.1016/j.combustflame.2015.11.004.
[78] Kéromnès A, Metcalfe WK, Heufer KA, Donohoe N, Das AK, Sung C-J, Herzler J, Naumann C, Griebel P, Mathieu O, Krejci MC, Petersen EL, Pitz WJ, Curran HJ. An experimental and detailed chemical kinetic modeling study of hydrogen and syngas mixture oxidation at elevated pressures. Combust Flame 2013;160(6):995–1011. https://doi.org/10.1016/j.combustflame.2013.01.001.
[79] Lindstedt R, Meyer M. A dimensionally reduced reaction mechanism for methanol oxidation. Proc Combust Inst 2002;29(1):1395–402. https://doi.org/10.1016/s1540-7489(02)80171-7.
[80] Wang H, Ra Y, Jia M, Reitz RD. Development of a reduced n-dodecane-PAH mechanism and its application for n-dodecane soot predictions. Fuel 2014;136:25–36. https://doi.org/10.1016/j.fuel.2014.07.028.
[81] Bagheri G, Ranzi E, Pelucchi M, Parente A, Frassoldati A, Faravelli T. Comprehensive kinetic study of combustion technologies for low environmental impact: MILD and OXY-fuel combustion of methane. Combust Flame 2020;212:142–55. https://doi.org/10.1016/j.combustflame.2019.10.014.
[82] Pei Y, Mehl M, Liu W, Lu T, Pitz WJ, Som S. A multicomponent blend as a diesel fuel surrogate for compression ignition engine applications. J Eng Gas Turbines Power May 2015;137(11). https://doi.org/10.1115/1.4030416.
[83] Lu T, Law CK. Strategies for mechanism reduction for large hydrocarbons: n-heptane. Combust Flame 2008;154(1–2):153–63. https://doi.org/10.1016/j.combustflame.2007.11.013.